PHYSICAL REVIEW FLUIDS **11**, 053601 (2026)

Bubble dissolution kinetics in porous media

Yuehongjiang Yu,[1] Yang Yang,[1] Jie Qi,[1] Yu Qiu,[2] Mengdi Sun,[3] and Ke Xu[1,4,*]
[1]*School of Mechanics and Engineering Science, Department of Energy and Resources Engineering, Peking University, Beijing 100871, China*
[2]*Department of Energy Science & Engineering, Stanford University, Stanford, California 94305-2220, USA*
[3]*National Key Laboratory of Continental Shale Oil, Northeast Petroleum University, Daqing 163318, China*
[4]*Research Institute of Extraterrestrial Material, Peking University, Beijing 100871, China*

(Received 1 January 2026; accepted 10 April 2026; published 1 May 2026)

The dissolution of trapped bubbles in porous media plays a key role in subsurface gas storage, groundwater ecology, and multiphase chemical reactors. We demonstrate that the classic Epstein-Plesset model for bubble dissolution in open space fails in porous media, because pore-throat geometry (1) decouples the characteristic diffusion distance and effective mass transfer area from the bubble size and (2) distorts concentration field near bubble surface. We propose kinetic dissolution theories with analytical solutions, validated through numerical simulations and microfluidic experiments. Our results provide physical mechanisms for the predictive modeling of bubble dissolution in diverse porous media.

DOI: 10.1103/jr19-lxmr

I. INTRODUCTION

Bubbles in porous media are prevalent across various fields, including geological storage [1,2], hydrological transport [3–5], chemical engineering processes [6], and electrochemical systems [7,8]. Typical examples include *in situ* bubble generation during pressure relief in oil wells [9], carbon dioxide bubbles produced by microbial degradation of organic matter in groundwater [10], and oxygen bubbles formed during charge-discharge cycles in zinc-air batteries [7]. Following their formation, bubbles may gradually dissolve into the surrounding liquid within the porous matrix, and their dissolution kinetics profoundly influence the efficiency and stability of the associated processes. Specifically, the dissolution rate of CO_2 bubbles is directly linked to the long-term security of geological carbon sequestration projects [11–15], while in groundwater remediation, dissolution kinetics governs the transport and removal efficiency of gaseous contaminants [16]. Therefore, a thorough investigation of bubble dissolution kinetics in porous media is of great importance to various technologies related to environmental protection and energy storage and extraction.

Nevertheless, a kinetic theory of bubble dissolution in porous media is still lacking. Much of the research follow the Epstein-Plesset (E-P) model [17–19], a classic theory derived for bubbles in open spaces without geometric confinement [20–22]. Jia *et al.* conducted experiments to measure the dissolution rate and pointed out that the E-P model significantly overestimated the measured data [18]. This discrepancy is attributed to the restriction of mass transfer pathways imposed by the porous medium. Jiang *et al.* experimentally demonstrated the influence of pore-throat size on the dissolution pathways of bubbles in porous media [23]. In addition, Zhai *et al.* found that the dissolution rate of bubbles in porous media is positively correlated with pore connectivity [24]. These studies qualitatively highlighted the critical role of porous structure on bubble dissolution

---

[*] Contact author: kexu1989@pku.edu.cn

TABLE I. Key geometric parameters and fluid parameters in microfluidic experiments.

Pore radius R_p (μm)	Throat length L_t (μm)	Throat width W_t (μm)	Diffusion coefficient of air in decane, D (m^2/s)	Air solubility in decane, c_s (mol/m^3)
240	420	76	6.40×10^{-9}	5.50 [42]

rate. However, a quantitative theory of how porous structure reshapes bubble dissolution remains largely unexplored.

Here we conduct microfluidic experiments and numerical simulations to reveal the role of porous structure and bubble morphology on dissolution kinetics. We consider bubbles of three commonly observed morphologies: (1) single-pore bubbles, that is, confined in one pore body, typically formed by chemical reactions [25–27], hydraulic snap-off [28], or direct bubble injection [29,30]; (2) linear (strip-shaped) bubbles, usually generated by unidirectional pressure-driven displacement [31,32]; and (c) block-shaped (roughly isotropic) bubbles, often produced by the massive exsolution of dissolved gases due to pressure relief in geological formations [33,34], continuous gas injection [27,30], or wetting-phase imbibition [35]. We derive analytical solutions for each type of morphology and propose a reasonable strategy for modeling and predictions in more complicated cases.

II. MICROFLUIDIC EXPERIMENT

A. Experiment methods

Transparent microfluidic chips are fabricated using standard soft lithography, in which NOA81 (Norland Adhesive 81) is the material directly contacting fluids. NOA81 is resistant to organic solvents, stable for surface treatments [36], making it widely applied in diverse microfluidic applications [37–39]. We use identical cylindrical arrays to simulate a homogeneous porous structure. As for fluid systems, we use degassed decane as the continuous phase and air as the discrete gas phase. Since oxygen and nitrogen are of very close solubility and diffusivity in liquid and are commonly treated as one component in many dissolution experiments [40,41], we treat air as a single component and use uniform solubility and diffusion coefficient. The advantages of this system are (1) a moderate dissolution rate which allows for direct observations and (2) no chemical reaction between the gas and the solution. During the experiment, we first inject air-in-decane bubbles in the media and then displace with degassed decane. The injection of degassed decane is stopped when only one bubble remains in the system, and the dissolution process is recorded using time-lapse photography. The distance between the dissolving bubble and the system boundary is at least ten times the bubble radius, and the total gas dissolution capacity of the surrounding fluid is much larger than the mass of the gas bubble, allowing us to treat this system as infinitely large. As capillary pressure for bubbles above micrometer size is much smaller than ambient pressure, we neglect the extra solubility due to surface curvature. The microfluidic geometric parameters and key thermodynamic properties are detailed in Table I (under normal temperature and pressure conditions). As the gap thickness is much smaller than the pore scale, we treat the bubbles in the chip as 2D, which allows us to write the volume of a single pore as $V_p = \pi R_p^2$, the cross-sectional area of a throat as $A_t = W_t$, and the volume of a throat as $V_t = L_t W_t$.

B. Experimental results

Bubbles in porous media have complex morphology, and the effect of bubble morphology on dissolution kinetics cannot be ignored [43]. Therefore, we conducted microfluidic experiments for all three types of bubbles (single-pore bubble, linear bubble, and block-shaped bubble). We characterize the dissolution kinetics in Figs. 1(a)–1(c). For each type of bubble, we conducted

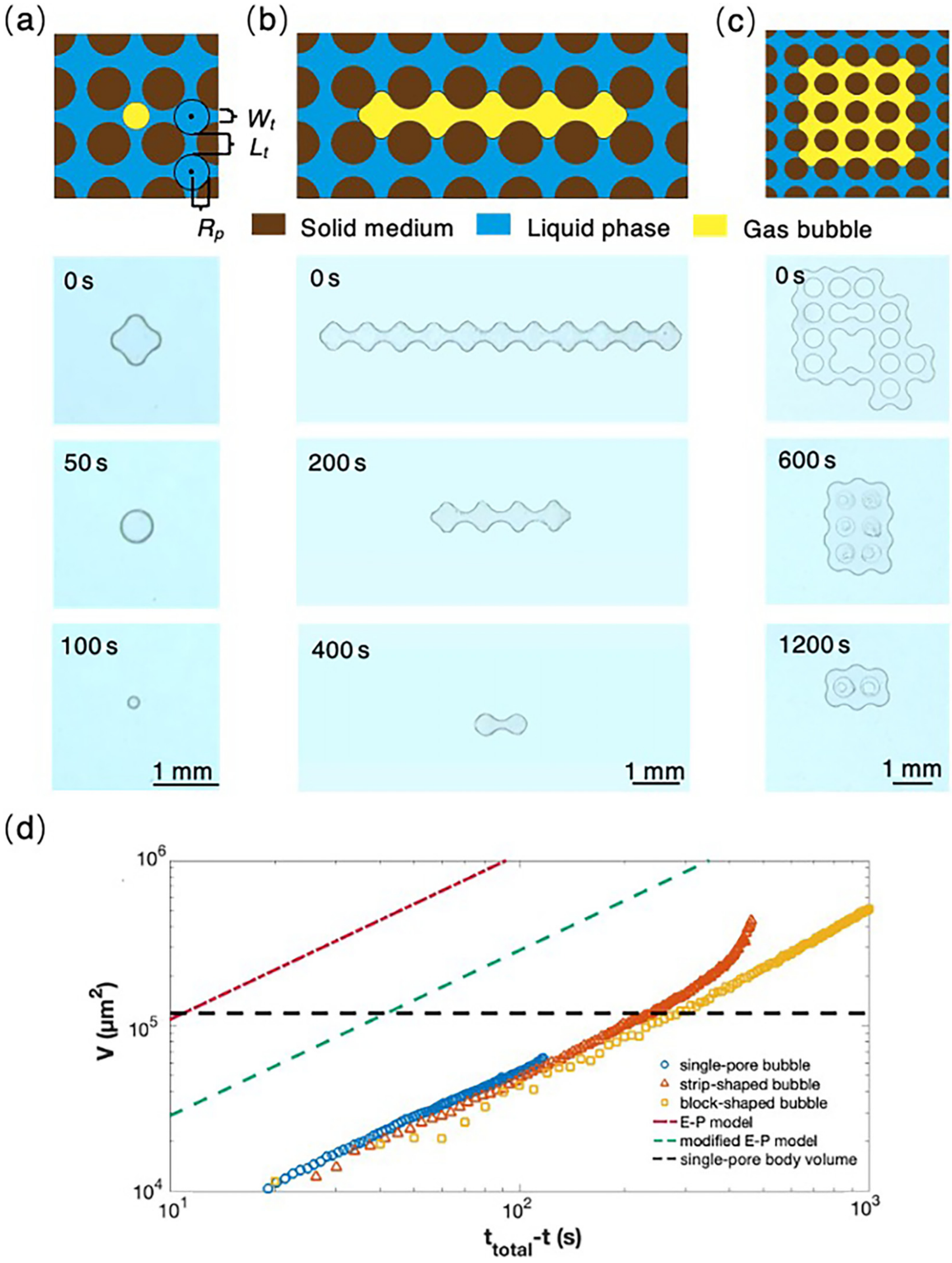

FIG. 1. Bubbles of different morphologies dissolving in porous media. (a)–(c) Different bubble morphologies in microfluidic experimental images: (a) single-pore bubble, (b) strip-shaped bubble, and (c) block-shaped bubble. (d) Microfluidic experimental bubble dissolution rate compared with the E-P model and modified E-P model. The single-pore body volume refers to the threshold volume: when a bubble's volume is smaller than this value, it is a single-pore bubble.

repeated experiments to ensure the accuracy and reliability of the data. Note that the pore-network in microfluidic experiments is 2D.

Figure 1(d) shows the experimental bubble dissolution results, where V is the bubble volume, t_{total} is the total dissolution time. and t is the dissolution time. The experimental bubble dissolution results significantly deviate from the E-P model, and the modified model using classic prefactor for mass transfer in porous media $\emptyset/\tau$ ($\emptyset = 0.38$ is porosity and $\tau = 1.43$ is tortuosity) largely overestimates the dissolution rate [44]. Single-pore bubbles and block-shaped bubbles still follow linear volume-time scaling as that in E-P model but are of much lower rates; strip-shaped bubbles follow very different and nonlinear dissolution kinetics.

III. NUMERICAL SIMULATIONS

Microfluidic experiments are confined to 2D networks. They can provide valuable data for qualitative phenomena as well as for calibration of key data, but cannot provide precise concentration field as well as the dynamics in 3D pore networks. To support in-depth theoretical analysis with more details as well as to extend the study to 3D networks, we first revisit the derivation of the E-P model and its underlying assumptions, and then establish efficient numerical simulation tools.

A. Revisiting Epstein-Plesset model

Governing equation for ideal-gas bubble volume reduction during dissolution in isotropic open-space environment is written as [45]

$$\frac{dV}{dt} = -k_0 D S \left(\frac{\partial c}{\partial r}\right)_{r=R_b}, \tag{1}$$

where $k_0 = \frac{RT}{P_0}$, R is the gas constant, T is temperature, P_0 is ambient pressure, S is mass transfer area, which is the bubble's surface area, R_b is bubble radius, c is solute concentration, and $(\frac{\partial c}{\partial r})_{r=R_b}$ characterizes the driving force of mass transfer near bubble surface, which is written in the E-P model as

$$\left(\frac{\partial c}{\partial r}\right)_{r=R_b} = c_s\left[\frac{1}{R_b} + \frac{1}{(\pi D t)^{\frac{1}{2}}}\right], \tag{2}$$

where c_s is saturated concentration. Considering the quasi-static-state situation that $\frac{1}{R_b} \gg \frac{1}{(\pi D t)^{1/2}}$ (applicable for bubbles discussed in this paper; see the Supplemental Material (SM) S1 for a detailed demonstration [46]), $(\frac{\partial c}{\partial r})_{r=R_b} = \frac{c_s}{R_b}$, substituting this into Eq. (1), we get

$$\frac{dV}{dt} = -k_0 D S_b \frac{c_s}{R_b}. \tag{3}$$

In the 2D case, $S_b \sim R_b$, so integrating Eq. (3) yields $V \sim t$. In the 3D case, $S_b \sim R_b^2$, so integrating Eq. (3) yields $V^{\frac{2}{3}} \sim t$.

From Eq. (3), we identify two key factors affecting the bubble dissolution rate: (1) the characteristic mass transfer distance, which is the radius of the bubble itself (R_b) in open space, and (2) the mass transfer area, which is the surface area of the bubble (S_b) in open space. Both of them keep changing during bubble dissolution. The evolution of these two factors in porous media may be largely different from that in open space as assumed in the E-P model.

B. Pore-scale diffusion mechanisms and assumptions

To capture the difference of mass transfer distance and mass transfer area between porous media in open space at quasi-steady state, we numerically simulate the dimensionless concentration field (c/c_s) of the diffusion process of a fixed-size and fixed-concentration source in a porous medium

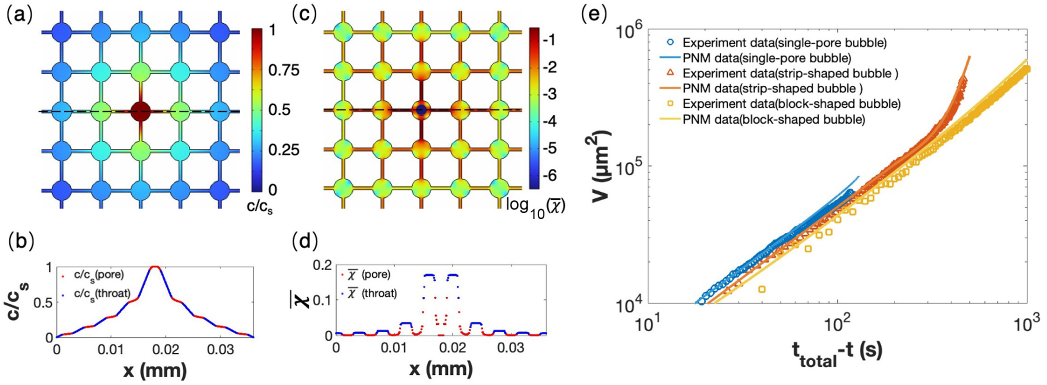

FIG. 2. (a) Dimensionless concentration field simulation for fixed-source diffusion in porous media. (b) Dimensionless dissipation rate field simulation for fixed-source diffusion in porous media. (c) Variation of dimensionless concentration along the dashed centerline in (a). (d) Variation of dimensionless dissipation rate along the dashed centerline in (c). (e) Comparison between microfluidic experimental results and PNM results for 2D bubble dissolution rate in porous media.

[Fig. 2(a)], and characterize the dimensionless dissipation rate field $\bar{\chi} = \frac{(\nabla c)^2}{(c_s/L_t)^2}$ [Fig. 2(b)] using COMSOL Multiphysics, where $\bar{\chi}$ characterizes the attenuation rate of the mass transfer driving force [47,48]. The radius of this source is half of the pore radius and has always maintained a saturated concentration, and boundary concentration is fixed at $c = 0$. The simulation results show that mass transfer quickly reaches a quasi-steady state (in less than 0.1 sec), and Figs. 2(a)–2(d) present the situation at $t = 1s$. See SM S2 [46] for detailed simulation parameters. Figure 2(c) presents the variation of dimensionless concentration [along the dashed centerline in Fig. 2(a)] within pores and throats, while Fig. 2(d) presents the variation of dimensionless dissipation rate [along the dashed centerline in Fig. 2(c)] across pores and throats.

Figures 2(a)–2(d) shows that porous structure does significantly distort the mass transfer near the bubble surface: the concentration of solute in each pore body is almost uniform, while the mass transfer hot spots uniformly distribute along each throat. It echoes earlier general studies on mass transfer in a pore network [49,50] that mass transfer is limited by throats under negligible bulk advection.

Therefore, both characteristic diffusion length and effective mass transfer area during bubble dissolution are regulated by the porous structure, instead of by a bubble's intrinsic morphologic parameters such as those in the E-P model:

(1) The characteristic mass transfer distance is no longer the radius of the bubble (R_b) itself, but regulated and discretized by throat with length L_t.

(2) The effective mass transfer area S is no longer the surface area of the bubble, but the sum of the cross-sectional areas of the throats connecting neighboring bubble-free pores.

C. Pore-network modeling (PNM) methods

The above simulation results allow the assumption that solute concentration within each pore is uniform and along a throat is linearly distributed during the bubble dissolution process in porous media. Therefore, we apply a recently developed PNM framework to facilitate the investigation of bubble dissolution kinetics in porous media [51,52]. In this model, the complex void geometry of a porous medium is represented by an interconnected network of pores and throats, where diffusion adheres to Fick's law, gas solubility follows Henry's law, and constant concentration boundary conditions are imposed. For the purposes of this study, two sets of different parameters are used in the simulations: set-Exp is identical to the parameters of our microfluidic experiments (as shown in Table I), and set-Ideal is of long and narrow throats to comply with abovementioned assumptions as much as possible. Detailed parameters of the simulation are listed in SM S3 [46]. This model has been validated by multiple recent micromodel experiments [40], and we further verified its reliability by conducting PNM simulations using the same parameters as those in Table I. As shown in Fig. 2(e), our PNM well reproduces the dissolution rates of different bubbles observed in the microfluidic experiments.

IV. THEORIES

Our previous derivation has demonstrated that bubble dissolution in porous media exhibits two key deviations from the E-P model for open spaces: (1) the key factor governing characteristic mass transfer shifts from the bubble radius R_b to a function of throat length L_t and (2) the mass transfer area S changes from the bubble's surface area to the sum of the cross-sectional areas of the throats connecting the adjacent pores. Porous structure thus discretizes the concentration field near bubble surface, and Eq. (1) can be rewritten as

$$\frac{dV}{dt} = -k_0\, D\, nA_t\, \frac{c_s - \overline{c_i}}{L_t}, \tag{4}$$

where n is the number of throats that connect pores containing bubble with unsaturated adjacent pores, highly related to bubble morphology, and $\overline{c_i}$ is the average concentration of all adjacent pores. In Eq. (4) morphology of bubble determines both n and $\overline{c_i}$.

Note that dissolution in porous media is significantly slower than that in open space as that assumed in the E-P model, so we still assume a quasi-steady state as that in E-P model. We consider bubbles in porous media with three types, and discuss the 2D and 3D scenarios separately. We considered only a homogeneous porous structure for achieving analytical solutions.

A. Single-pore bubble

For single-pore bubbles, the pore occupancy does not change during the dissolution process. Therefore:

(1) The mass transfer is through pore throats of a constant number $n = n_1$, so effective mass transfer area S is a constant.

(2) According to the quasi-steady-state assumption, $c_s - \overline{c_i} = \varepsilon c_s$ remains constant during dissolution if the pore occupancy does not change, and the value of the constant ε is jointly determined by the bubble morphology and pore geometry. We verify this assumption using PNM simulation results (a detailed explanation is provided in SM 4.1 [46]).

Substituting n and $\overline{c_l}$ into Eq. (4) and integrate, we get a proportional scaling for the dissolution of a bubble occupying a single pore:

$$V_0 - V = F_{\text{single}} F_0 t, \tag{5}$$

where V_0 is the initial bubble volume, $F_{\text{single}} = \frac{n_1 \varepsilon A_t}{L_t}$ is a geometric prefactor determined only by the geometric properties of the porous medium, and $F_0 = \frac{RTDc_s}{P_0}$ is a thermodynamic prefactor, determined by fluid properties. Accordingly, total dissolution time for a single-pore bubble is $V_0/F_{\text{single}}F_0$. We achieve the value of ε for both 2D and 3D networks with an approximation method using Taylor series approximation (detailed derivation of ε is provided in SM 4.1 [46]). For the 2D case, $n_1 = 4$, $\varepsilon = 0.466$; for the 3D case, $n_1 = 6$, $\varepsilon = 0.691$.

For the 2D case, we compared the microfluidic experimental data with an analytical solution and PNM simulation results as shown in Figs. 2(e) and 3(a). It validates both the PNM model and the analytical solution. Figure 3(b) presents multiple sets of total dissolution times from PNM simulations in comparison with the theoretical solution, using both set-Exp and set-Ideal. It is worth noting that the total dissolution times obtained from our PNM simulations are often slightly shorter than the theoretically predicted values. We attribute this to the fact that the dissolution rate of bubbles

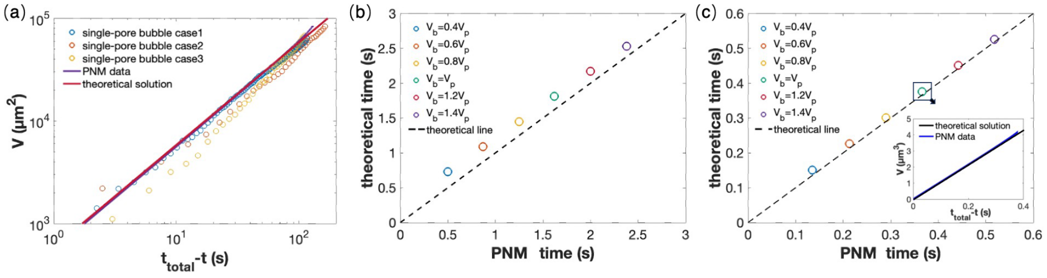

FIG. 3. (a) Microfluidic experiments and PNM data of single-pore bubble's volume change over time compared with theoretical solution of single-pore bubble dissolution. (b) Nine sets of 2D total bubble dissolution times from PNM simulations (with varied initial bubble volumes) are compared with the theoretical results, where open symbols correspond to simulations using set-Ideal, and filled symbols correspond to those using set-Exp. (c) Six sets of 3D total dissolution times of bubbles from PNM simulations (with varied initial bubble volumes) compared with the theoretical results, where the zoomed-in section shows the time-dependent volume change image of the entire bubble dissolution process.

at the initial stage is significantly faster than the theoretical prediction, which stems from the solution concentration field around the bubbles not yet having reached the quasi-steady state we assumed.

As the microfluidic experiments well validate the PNM, we extend them to the 3D case and compare the results of an analytical solution with multiple sets of data from PNM simulations as illustrated in Fig. 3(c). They agree even better than those in 2D cases. All numerical simulation parameters are presented in SM S3 [46].

B. Strip-shaped bubble

For the strip-shaped bubble, the pore occupancy does change during the dissolution process. Nevertheless, if we treat it as an infinitely long bubble chain, the dissolution becomes completely determined by the mass transfer in the plane perpendicular to the bubble chain. On such a plane, the pore occupancy is constantly one, as a single-pore bubble in a reduced dimension case. Therefore:

(1) All pores containing bubbles are directly connected to the external unsaturated pores, $n = n_1 \frac{V}{V_p+V_t}$.

(2) According to the quasi-steady-state assumption, $c_s - \overline{c_i} = \varepsilon c_s$ remains constant during dissolution if the pore occupancy does not change. We verify this inference using PNM simulation results (detailed explanation is provided in SM 4.2 [46]).

Substituting n and $\overline{c_l}$ into Eq. (4) and integrating, we get

$$\ln{(V/V_0)} = -F_{\text{strip}} F_0\, t, \tag{6}$$

where $F_{\text{strip}} = \frac{n_1 \varepsilon A_t}{L_t(V_p+V_t)}$ is a prefactor determined only by the geometric properties. We estimate the total dissolution time as $\ln(V_0/V_{\text{pore}})/F_{\text{strip}}F_0 + V_{\text{pore}}/F_{\text{single}}F_0$, where the first term is the time for a strip-shape bubble evolves into a single-pore bubble, while the second term is the time for a single-pore bubble to fully dissolve. We achieve the value of ε for both 2D and 3D networks by an approximation method. For the 2D case, $n_1 = 2$, $\varepsilon = 0.182$; for the 3D case, $n_1 = 4$, $\varepsilon = 0.322$(detailed derivation of ε is provided in SM 4.2 [46]).

For the 2D case of strip-shaped bubbles, comparisons between the analytical solution, microfluidic experimental data, and PNM simulation results are shown in Figs. 2(e) and 4(a). The analytical solution matches well both microfluidic experiments and PNM simulations. It validates both the PNM model and the analytical solution. Figure 4(b) presents PNM-derived total dissolution times versus the theoretical solution using both set-Exp and set-Ideal, with simulated times slightly shorter than predicted—still attributed to the initial faster dissolution before the surrounding concentration field reaches the assumed quasi-steady state.

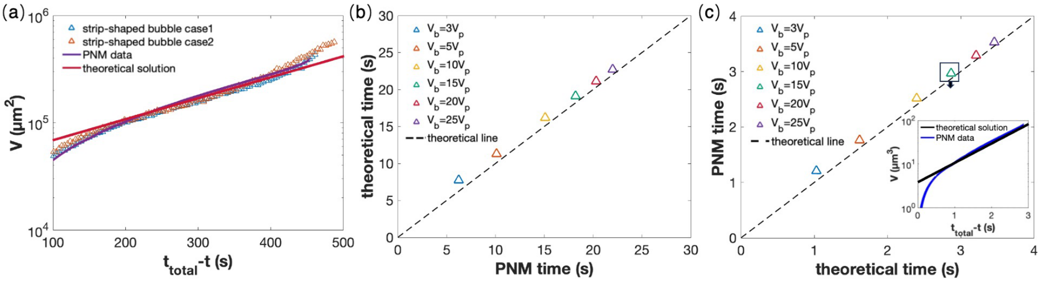

FIG. 4. (a) Microfluidic experiments and PNM data of a strip-shaped bubble's volume change over time compared with theoretical solution of strip-shaped bubble dissolution. (b) Nine sets of 2D total dissolution times of strip-shaped bubbles from PNM simulations (with varied initial bubble volumes) compared with the theoretical results, where open symbols correspond to simulations using set-Ideal, and filled symbols correspond to those using set-Exp. (c) Six sets of 3D total dissolution times of strip-shaped bubbles from PNM simulations (with varied initial bubble volumes) compared with the theoretical results, where the zoomed-in section shows the time-dependent volume change image of the entire bubble dissolution process.

As the microfluidic experiments well validate the PNM, we extend them to the 3D case, and good agreement between the analytical solution and PNM simulation data [Fig. 4(c)] further validates the theory for 3D strip-shaped bubbles. All numerical simulation parameters are presented in SM S3 [46].

C. Block-shaped bubble

For the block-shaped bubble, as the bubble radius R_b continuously decreases during the dissolution process in all dimensions, the pore occupancy can no longer be considered unchanged. If the bubble is much larger than pore unit, the E-P model with diffusivity modified by porous geometry may still be valid. However, if the bubble size is still comparable to the pore structure, pore-throat geometry can still largely distort the near-interface concentration field and the dissolution kinetics.

The critical bubble size for a block-shaped bubble can be determined by equating the characteristic diffusion length for E-P model and the throat length L_t. The former can be estimated by modifying that of E-P in open space, R_b, with the reduction rate of diffusion coefficient, ϕ/τ, as $R_b\phi/\tau$. The critical bubble size is therefore $L_t\tau/\phi$. For the set-Exp, this critical bubble radius is approximately $4L_t$ in 2D, while for our ideal parameters, it is smaller than $0.1R_b$ in two dimensions. Therefore, for both the bubbles in our microfluidic experiment ($R_b < 4L_t$) and those in the numerical simulations using set-Ideal ($R_b < 10L_t$), the characteristic mass transfer distance is smaller than the throat length L_t. Under such a condition, the existence of the throat fixes the characteristic diffusion length to L_t, while the effective surface area does changes during the dissolution:

(1) Only the pores containing the outermost part of the bubble can transfer mass with the external solution via the throat. Thus, n is proportional to the number of pores occupied by the bubble's outermost layer, which is in turn proportional to the bubble's surface area, so $n \sim R_b^{d-1} \sim V^{1-1/d}$. Exact derivation yields $n = n_1(\frac{V}{V_p+dV_t})^{1-1/d}$.

(2) Since the characteristic mass transfer distance remains unchanged, we can still adapt the quasi-steady-state assumption, and $c_s - \overline{c_i} = \varepsilon c_s$ remains constant during dissolution. We verify this inference using PNM simulation results (a detailed explanation is provided in SM 4.3 [46]).

Substituting n and $\overline{c_l}$ into Eq. (4) and integrating, we get

$$V_0^{\frac{1}{d}} - V^{\frac{1}{d}} = F_{\text{block}} F_0 t, \tag{7}$$

where $F_{\text{block}} = \frac{n_1 \varepsilon A_t}{d(V_p+dV_t)^{1-1/d} L_t}$ is the geometric prefactor determined only by the geometric properties of the porous medium. The total dissolution time can be estimated as $V_0^{\frac{1}{d}}/F_{\text{block}}F_0$. We achieve the

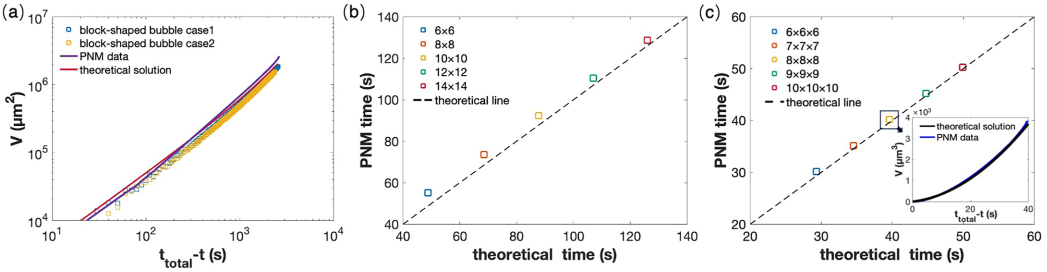

FIG. 5. (a) Microfluidic experiments and PNM data of a block-shaped bubble's volume change over time compared with theoretical solution of block-shaped bubble dissolution. (b) Ten sets of 2D total dissolution times of block-shaped bubbles from PNM simulations (with varied initial bubble volumes) compared with the theoretical results: all the initial bubbles are set to be square, the open symbols correspond to simulations using set-Ideal, and filled symbols correspond to those using set-Exp. (c) Five sets of 3D total dissolution times of block-shaped bubbles from PNM simulations (with varied initial bubble volumes) compared with the theoretical results, where the zoomed-in section shows the time-dependent volume change image of the entire bubble dissolution process, and all the initial bubbles are set as cubes.

value of ε for both 2D and 3D networks by an approximation method. For the 2D case, $n_1 = 4$, $\varepsilon = 0.157$; for the 3D case, $n_1 = 6$, $\varepsilon = 0.361$ (detailed derivation of ε is provided in SM 4.3 [46]).

For the 2D case of block-shaped bubbles, comparisons between the analytical solution, microfluidic experimental data, and PNM simulation results are shown in Figs. 2(e) and 5(a). The analytical solution matches well both microfluidic experiments and PNM simulations. It validates both the PNM model and the analytical solution. Figure 5(b) presents PNM-derived total dissolution times versus the theoretical solution, where it is shown that for set-Ideal cases, the simulated times well match the theory. However, for the set-Exp cases, once the bubble is larger than 7×7 (whose bubble radius is $4L_t$), the characteristic mass transfer distance exceeds L_t, and the dissolution time simulated by PNM deviates rapidly from the theoretical value, as we discussed in the beginning of this section.

We extend to the 3D case, and good agreement between the analytical solution and PNM simulation data [Fig. 5(c)] further validates the theory for 3D strip-shaped bubbles. All numerical simulation parameters are presented in SM S3 [46].

V. IMPLICATIONS AND LIMITATIONS

We demonstrate that bubble morphology exerts a significant influence on the dissolution scaling law of bubbles in porous media, with the dissolution rate of bubbles of the same volume potentially differing by orders of magnitude. For example, for a bubble with a volume 25 times the single-pore body volume under set-Exp parameters, a block-shaped bubble requires nearly five times as long to fully dissolve as a strip-shaped bubble, as predicted by Eqs. (6) and (7). As a result, although bubble dissolution in a fixed ambient condition is only a function of initial bubble size in open space as predicted by the E-P model; additional information (such as bubble morphology) is needed for a reasonable prediction of that in porous media. Unfortunately, existing studies on bubble dissolution in porous media primarily focus on gas saturation and overlook bubble morphology information [53] which needs further investigation to establish a comprehensive dissolution model. Our theory also provides references for morphology-dependent dissolution prefactors for other mass transfer processes (such as macroscopic depletion processes [54]) in porous media.

To derive analytical solutions, this work focuses on the dissolution behavior of a single bubble of three types of morphologies in homogeneous porous media. This idealized scenario provides a foundational framework, while real-world systems involve additional complexities. For bubble dissolution in heterogeneous porous media, while heterogeneity may be averaged out in the far field, it is important in the near field, likely to affect the dissolution rate as well as the pore-by-pore retraction trajectory. Furthermore, the connectivity of block-shaped bubbles may also influence the retraction trajectory, and their morphological characterization constitutes a complex system that requires the introduction of additional parameters (such as the Euler characteristic) for adequate description [55]. Therefore, discussions of heterogeneity and complex bubble morphologies represent important directions for the development of our theory. Additionally, our analysis is confined to bubbles larger than the micrometer scale, thus neglecting the effect of varying capillary pressure on gas solubility, and future research should address the influence of capillary pressure on bubble dissolution kinetics.

VI. CONCLUSION

Our work demonstrates the presence of porous structure fundamentally changes the bubble dissolution dynamics via the control of the mass transfer process, which is far beyond a simple coefficient correlation.

We systematically elucidated the physical mechanisms underlying the effect of porous media on bubble dissolution kinetics through a combination of microfluidic experiments, PNM simulations, and theoretical derivations. Our results reveal two core reasons for the failure of the classic E-P model in porous media: (1) the characteristic mass transfer distance is no longer determined by the bubble radius but is instead governed by the pore-throat structure and (2) the effective mass transfer area is no longer the bubble's surface area but the sum of the cross-sectional areas of throats connecting the bubble-containing pores to unsaturated adjacent pores, with this area varying significantly based on bubble morphology.

For the three typical bubble morphologies (single-pore, strip-shaped, and block-shaped) observed in porous media, we derived corresponding analytical solutions for their dissolution kinetics in both 2D and 3D scenarios. These theoretical results are well validated by our microfluidic experimental data and PNM simulations, confirming the reliability of the proposed framework.

Experiments, numerical simulations, and analytical solutions confirm that bubble morphology is a key parameter to determine their dissolution behavior in porous media. Classic models considering only bubble volume need modification.

The findings provide critical theoretical support for optimizing key engineering applications, including the long-term security of geological carbon sequestration (by improving predictions of CO_2 bubble dissolution rates) and the efficiency of groundwater remediation (by enhancing the removal of gaseous contaminants).

ACKNOWLEDGMENTS

We gratefully acknowledge the financial support and funding provided by the National Key Research and Development Program of China (No. 2023FYA1011700), the National Natural Science Foundation of China (Grant No. U23B6004), and the China National Petroleum Corporation-Peking University Strategic Cooperation Project of Fundamental Research.

DATA AVAILABILITY

The data that support the findings of this article are openly available [56].

---

[1] H. E. Huppert and J. A. Neufeld, The fluid mechanics of carbon dioxide sequestration, Annu. Rev. Fluid Mech. **46**, 255 (2014).

[2] S. M. Benson and F. M. Orr, Carbon dioxide capture and storage, MRS Bull. **33**, 303 (2008).

[3] J. Holocher, F. Peeters, W. Aeschbach-Hertig, W. Kinzelbach, and R. Kipfer, Kinetic Model of gas bubble dissolution in groundwater and its implications for the dissolved gas composition, Environ. Sci. Tech. **37**, 1337 (2003).

[4] C. T. Miller, M. M. Poirier-Mcneill, and A. S. Mayer, Dissolution of trapped nonaqueous phase liquids: Mass transfer characteristics, Water Resour. Res. **26**, 2783 (1990).

[5] S. E. Powers, L. M. Abriola, and W. J. Weber, An experimental investigation of non- aqueous phase liquid dissolution in saturated subsurface systems: Steady state mass transfer rates, Water Resour. Res. **28**, 2691 (1992).

[6] C. Chang, Q. Zhou, T. J. Kneafsey, M. Oostrom, T. W. Wietsma, and Q. Yu, Pore-scale supercritical CO_2 dissolution and mass transfer under imbibition conditions, Adv. Water Res. **92**, 142 (2016).

[7] H. Al-Fetlawi, A. A. Shah, and F. C. Walsh, Modelling the effects of oxygen evolution in the all-vanadium redox flow battery, Electrochim. Acta **55**, 3192 (2010).

[8] L. Chen, Y. L. He, W. Q. Tao, P. Zelenay, R. Mukundan, and Q. J. Kang, Pore-scale study of multiphase reactive transport in fibrous electrodes of vanadium redox flow batteries, Electrochim. Acta **248**, 425 (2017).

[9] A. Patmonoaji and T. Suekane, Investigation of CO_2 dissolution via mass transfer inside a porous medium, Adv. Water Res. **110**, 97 (2017).

[10] M. L. Johns and L. F. Gladden, Magnetic resonance imaging study of the dissolution kinetics of octanol in porous media, Colloid Interface Sci. **210**, 261 (1999).

[11] W. Bohao, L. Xingbo, T. Ying, P. F. Lv, Y. Liu, T. T. Luo, J. A. Zheng, D. Y. Wang, and L. L. Jiang, Characterizing the dissolution rate of CO_2-brine in porous media under gaseous and supercritical conditions, Appl. Sci. **8**, 4 (2017).

[12] R. Moghadasi, S. Goodarzi, Y. Zhang, B. Bijeljic, M. J. Blunt, and A. Niemi, Pore-scale characterization of residual gas remobilization in CO_2 geological storage, Adv. Water Res. **179**, 104499 (2023).

[13] A. Patmonoaji, Y. Zhang, Z. Xue, H. Park, and T. Suekane, Experimental and numerical simulation of supercritical CO_2 microbubble injection into a brine-saturated porous medium, Int. J. Greenhouse Gas Control **91**, 102830 (2019).

[14] Z. Xue, T. Yamada, T. Matsuoka, H. Kameyama, and S. Nishio, Carbon dioxide microbubble injection—Enhanced dissolution in geological sequestration, Energy Procedia **4**, 4307 (2011).

[15] N. Joewondo, V. Garbin, and R. Pini, Experimental evidence of the effect of solute concentration on the collective evolution of bubbles in a regular pore-network, Chem. Eng. Res. Design **192**, 82 (2023).

[16] P. T. Imhoff, P. R. Jaffe, and G. F. Pinder, An experimental study of complete dissolution of a nonaqueous phase liquid in saturated porous media, Water Resour. Res. **30**, 307 (1994).

[17] Q. Gao, X. Jiang, Z. Wang, Z. X. Yang, J. Trivedi, X. G. Xu, A. O. Mmbuji, and V. Patel, CO_2 foam generation, propagation and decay characteristics: Recent advances and future perspectives with focus on CCUS implications, Fuel **389**, 134631 (2025).

[18] J. Haowei, Y. Haiyang, X. Feifan, Y. Zhou, X. Ke, and W. Yang, Research on CO_2 microbubble dissolution kinetics and enhanced oil recovery mechanisms, Chinese J. Theor. Appl. Mech. **55**, 755 (2023).

[19] N. Joewondo, V. Garbin, and R. Pini, Nonuniform collective dissolution of bubbles in regular pore networks, Transp. Porous Media **141**, 649 (2022).

[20] S. Zhao, Y. D. Ding, Q. Liao, X. Zhu, and Y. Huang, Experimental and theoretical study on dissolution of a single mixed gas bubble in a microalgae suspension, RSC Adv. **5**, 32615 (2015).

[21] V. R. Fanaie and M. Khiadani, Effect of salinity on air dissolution, size distribution of microbubbles, and hydrodynamics of a dissolved air flotation (DAF) system, Colloids Surf. A **591**, 124547 (2020).

[22] P. B. Duncan and D. Needham, Test of the Epstein−Plesset Model for gas microparticle dissolution in aqueous media: Effect of surface tension and gas undersaturation in solution, Langmuir **20**, 2567 (2004).

[23] L. Jiang, Z. Xue, and H. Park, Enhancement of CO_2 dissolution and sweep efficiency in saline aquifer by micro bubble CO_2 injection, Int. J. Heat Mass Transf. **138**, 1211 (2019).

[24] H. Zhai, Z. Xue, H. Park, Y. Aizawa, Y. Baba, and Y. Zhang, Migration characteristics of supercritical CO_2 microbubble flow in the Berea sandstone revealed by voxel- based X-ray computed tomography imaging analysis, J. Nat. Gas Sci. Eng. **77**, 103233 (2020).

[25] R. T. Amos and K. U. Mayer, Investigating the role of gas bubble formation and entrapment in contaminated aquifers: Reactive transport modelling, J. Contam. Hydrol. **87**, 123 (2006).

[26] K. A. Chang and W. B. Lindquist, The dynamics of gas-bubble formation at saturated conditions in porous media flow, Sci. Rep. **10**, 13175 (2020).

[27] B. Ghosh, A. Al-Hamairi, and S. Jin, Carbonated water injection: An efficient EOR approach. A review of fundamentals and prospects, J. Petrol. Explor. Prod. Technol. **10**, 673 (2020).

[28] Y. Tanino and M. J. Blunt, Capillary trapping in sandstones and carbonates: Dependence on pore structure, Water Resour. Res. **48**, W08525 (2012).

[29] L. Romero-Zerón and A. Kantzas, Pore-scale visualization of foamed gel propagation and trapping in a pore network micromodel, J. Can. Pet. Technol. **44**, 44 (2005).

[30] D. Wang, J. Fan, and Z. Xue, Hydrodynamic analysis of CO_2 migration in heterogeneous rocks: Conventional and micro-bubble CO_2 flooding experiments and pore-scale numerical simulations, Water Resour. Res. **58**, e2021WR031874 (2022).

[31] M. Clerget, A. Klimenko, M. Bourrel, F. Lequeux, and P. Panizza, Foam generation through a single pore with rectangular cross-section: Hysteretic behavior and geometric limitation of the volume fraction of bubbles, ACS Omega **9**, 8320 (2024).

[32] C. Wang and K. Xu, Ganglion startup in porous media, Chem. Eng. Sci. **292**, 119982 (2024).

[33] C. Garing, J. A. de Chalendar, M. Voltolini, J. B. Ajo-Franklin, and S. M. Benson, Pore-scale capillary pressure analysis using multi-scale X-ray microtomography, Adv. Water Res. **104**, 223 (2017).

[34] M. Andrew, B. Bijeljic, and M. J. Blunt, Pore-by-pore capillary pressure measurements using X-ray microtomography at reservoir conditions: Curvature, snap-off, and re-mobilization of residual CO_2, Water Resour. Res. **50**, 8760 (2014).

[35] Y. H. Xiao, Z. J. You, Z. T. Du, Y. M. He, J. Zheng, Y. J. Yuan, and L. Wang, Review on spontaneous imbibition mechanisms in gas-water systems: Impacts on unconventional gas production and CO_2 geo-sequestration, Gas Sci. Eng. **131**, 205466 (2024).

[36] P. Wägli, A. Homsy, and N. F. de Rooij, Norland optical adhesive (NOA81) microchannels with adjustable wetting behavior and high chemical resistance against a range of mid-infrared-transparent organic solvents, Sens. Actuators B **156**, 994 (2011).

[37] D. Bartolo, G. Degré, P. Nghe, and V. Studer, Microfluidic stickers, Lab Chip **8**, 274 (2008).

[38] B. Levaché and D. Bartolo, Revisiting the saffman-taylor experiment: Imbibition patterns and liquid-entrainment transitions, Phys. Rev. Lett. **113**, 044501 (2014).

[39] B. Levaché, A. Azioune, M. Bourrel, V. Studer, and D. Bartolo, Engineering the surface properties of microfluidic stickers, Lab Chip **12**, 3028 (2012).

[40] K. Xu, R. Bonnecaze, and M. Balhoff, Egalitarianism among bubbles in porous media: An Ostwald ripening derived anticoarsening phenomenon, Phys. Rev. Lett. **119**, 264502 (2017).

[41] Y. Qiu, X. W. Cai, X. Bian, and G. Hu, Design of a magnetically responsive artificial cilia array platform for microsphere transport, Lab Chip **25**, 330 (2025).

[42] R. Battino, T. R. Rettich, and T. Tominaga, The solubility of nitrogen and air in liquids, J. Phys. Chem. Ref. Data **13**, 563 (1984).

[43] P. Anindityo, T. Kento, M. Mushlih, and T. Suekane, Micro-tomographic analyses of specific interfacial area inside unconsolidated porous media with differing particle characteristics from microscopic to macroscopic scale, J. Colloid Interface Sci. **532**, 614 (2018).

[44] J. Bear, *Dynamics of Fluids in Porous Media* (American Elsevier, New York, 1972), pp. 132–133.

[45] P. S. Epstein and M. S. Plesset,On the stability of gas bubbles in liquid-gas solutions, Appl. Sci. Res. **19**, 256 (1951).

[46] See Supplemental Material at http://link.aps.org/supplemental/10.1103/jr19-lxmr for detailed verification of the quasi-steady-state assumption and key simulation parameters in COMSOL and PNM, which includes Ref. [45].

[47] R. S. Abiev, On the influence of the specific dissipation rate distribution on the efficiency of mass transfer in apparatuses with liquid-phase media, Processes **13**, 967 (2025).

[48] L. Chen and S. Xia, Minimum mass-entransy dissipation profile for one-way isothermal diffusive mass-transfer process with mass-resistance and mass-leakage, Sci. China Technol. Sci. **67**, 2427 (2024).

[49] Y. Yu, C. Wang, J. Liu, S. Mao, Y. Mehmani, and K. Xu, Bubble coarsening kinetics in porous media, Geophys. Res. Lett. **50**, e2022GL100757 (2023).

[50] Y. Mehmani, M. Oostrom, and M. T. Balhoff, A streamline splitting pore-network approach for computationally inexpensive and accurate simulation of transport in porous media, Water Resour. Res. **50**, 2488 (2014).

[51] Y. Mehmani and K. Xu, Capillary equilibration of trapped ganglia in porous media: A pore-network modeling approach, Adv. Water Res. **166**, 104223 (2022).

[52] Y. Mehmani and K. Xu, Pore-network modeling of Ostwald ripening in porous media: How do trapped bubbles equilibrate? J. Comput. Phys. **457**, 111041 (2022).

[53] P. Lv, Y. Chang, F. Liu, Y. Liu, B. Wang, X. Guo, and Y. Song, CO_2 brine mass transfer patterns and interface dynamics under geological storage conditions, Int. J. Heat Mass Transfer **222**, 125184 (2024).

[54] Y. Mehmani and K. Xu, A continuum theory of diffusive bubble depletion in porous media, Adv. Water Res. **185**, 104625 (2024).

[55] C. Wang, Y. Mehmani, and K. Xu, Capillary equilibrium of bubbles in porous media, Proc. Natl. Acad. Sci. USA **118**, e2024069118 (2021).

[56] Y. Yu, Y. Yang, J. Qi, Y. Qiu, M. Sun, and K. Xu, Experiment and simulation data for Bubble dissolution kinetics in porous media [Data set], Zenodo (2025), doi: 10.5281/zenodo.18098482.